J. Fluid Mech. (2014), *vol.* 749, *pp.* 627–648.
doi:10.1017/jfm.2014.230

First instability and structural sensitivity of the flow past two side-by-side cylinders

M. Carini[1], F. Giannetti[2] and F. Auteri[1],†

[1]Dipartimento di Scienze e Tecnologie Aerospaziali, Politecnico di Milano, via La Masa 34, 20156 Milano, Italy

[2]Dipartimento di Ingegneria Industriale, Università degli studi di Salerno, via Ponte don Melillo, 84084 Fisciano (SA), Italy

(Received 6 May 2013; revised 23 December 2013; accepted 21 April 2014; first published online 19 May 2014)

The onset of two-dimensional instabilities in the flow past two side-by-side circular cylinders is numerically investigated in the ranges $0.1 \leqslant g \leqslant 3$ and $Re < 100$, with g being the non-dimensional gap spacing between the surfaces of the two cylinders and Re the Reynolds number. A comprehensive, global stability analysis of the symmetric base flow is carried out, indicating that three harmonic modes and one steady antisymmetric mode become unstable at different values of g and Re. These modes are known to promote distinct flow regimes at increasing values of g: single bluff-body, asymmetric, in-phase and antiphase synchronized vortex shedding. For each mode, the inherent structural sensitivity is examined in order to identify the core region of the related instability mechanism. In addition, by exploiting the structural sensitivity analysis to base flow modifications, a passive control strategy is proposed for the simultaneous suppression of the two synchronized shedding modes using two small secondary cylinders. Its effectiveness is then validated *a posteriori* by means of direct numerical simulations.

Key words: instability control, separated flows, wakes/jets

1. Introduction

Flows past two or more cylinders in various arrangements have received considerable attention in the past. These flows are indeed prototypical of wake interference phenomena that can be found in many engineering applications such as heat exchangers, bridge pilings and off-shore platforms, among others. One of these prototypical configurations is represented by the flow past two identical circular cylinders in side-by-side arrangement which has been investigated extensively both in experiments and numerical simulations. Despite the simple geometry, it is known that the two cylinder wakes can experience complex interactions leading to several different flow patterns, see Sumner (2010) for a recent review. For this configuration the flow dynamics is governed by two parameters: the Reynolds number $Re = U^*_\infty D^*/\nu^*$ and the non-dimensional gap spacing between the two cylinder surfaces $g = g^*/D^*$ (see figure 1), being U^*_∞ the free-stream velocity, D^* the cylinder diameter and ν^* the kinematic viscosity.

† Email address for correspondence: franco.auteri@polimi.it

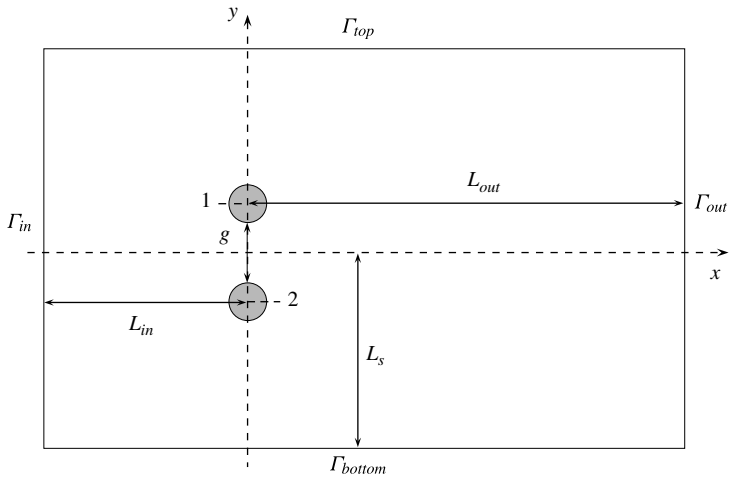

FIGURE 1. Sketch of the computational domain Ω_c employed for numerical investigations of the flow past two circular cylinders in side-by-side arrangement.

Most of the experimental works, from early research (Spivack 1946; Ishigai *et al.* 1972; Bearman & Wadcock 1973; Zdravkovich & Pridden 1977) to more recent investigations (Sumner *et al.* 1999; Zhou, Zhang & Yiu 2002; Alam, Moriya & Sakamoto 2003; Alam & Zhou 2007), have been carried out within the turbulent regime in the range of $10^3 \lesssim Re \lesssim 10^5$, where the occurrence of the various flow patterns is almost only determined by the gap spacing with minor effects due to the Reynolds number. It is well established (see for example Sumner *et al.* 1999; Kang 2003) that for such large Reynolds numbers and for $g \gtrsim 5$ wake coupling becomes negligible, leading to two nearly independent cylinder wakes. Under the above threshold, three main regimes are observed. When the two cylinders are in close proximity, i.e. $g \lesssim 0.2$, the flow behaves like that past a single bluff body with a characteristic length scale of $\sim 2D^*$ and a single von Kármán vortex street develops from the outer shear layers of the two cylinders. Differently, at large gap sizes, i.e. $g \gtrsim 1.2$, two parallel vortex streets are formed and synchronization of the double shedding process takes place either in phase or in phase opposition, with a predominance of this latter behaviour for $g \gtrsim 2$ (Williamson 1985; Zhou *et al.* 2002). Finally in the intermediate range $0.2 \lesssim g \lesssim 1.2$ wake patterns become distinctly asymmetric, being characterized by a biased gap flow toward one cylinder side. In addition, within this regime, the so-called flip-flopping behaviour of the gap flow is also observed (see Kang 2003; Sumner 2010, for details). At low Reynolds numbers a new explanation of the flip-flopping behavior has been recently described by Carini *et al.* (2014) who used Floquet analysis to show that this phenomenon is triggered by a secondary instability of the periodic in-phase base flow.

Numerical investigations have been performed using two-dimensional direct numerical simulations (DNS) (Meneghini *et al.* 2001; Jester & Kallinderis 2003; Kang 2003; Liu *et al.* 2007) as well as large eddy simulations (Chen, Tu & Yeoh 2003; Shao & Zhang 2008; Afgan *et al.* 2011) and in both cases a behaviour similar to those observed in the experiments was reproduced. At low Reynolds numbers, the occurrence of different flow regimes has been extensively investigated by Kang (2003) using an immersed-boundary finite difference technique. Within the ranges of $g \leqslant 5$

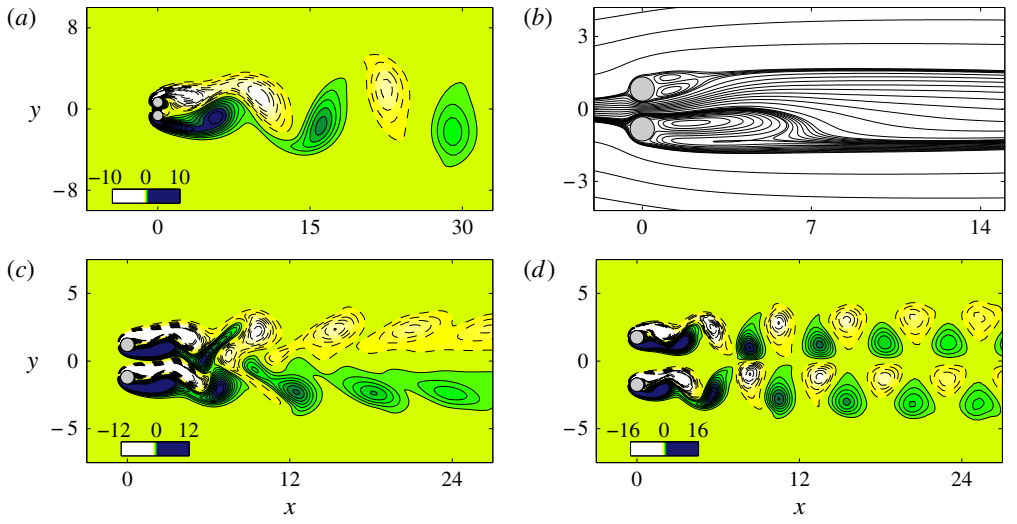

FIGURE 2. (Colour online) Flow snapshots (DNS). (*a*) 'Single bluff-body' flow at $g = 0.3$ and $Re = 30$ (vorticity field). (*b*) Asymmetric steady flow at $g = 0.65$ and $Re = 60$ (streamlines). (*c*) In-phase synchronized vortex shedding at $g = 1.4$ and $Re = 60$ (vorticity field). (*d*) Antiphase synchronized vortex shedding at $g = 2.5$ and $Re = 80$ (vorticity field).

and $40 \leqslant Re \leqslant 160$, Kang (2003) has identified six different wakes patterns: antiphase synchronized ($g \geqslant 2$), in-phase synchronized ($g \geqslant 1.5$), flip-flopping ($0.4 \leqslant g \leqslant 1.5$), single bluff-body ($g \leqslant 0.4$), deflected oscillatory ($50 \leqslant Re \leqslant 110$ and $0.2 \leqslant g \leqslant 1$) and steady symmetric ($Re \leqslant 40$ and $g \geqslant 0.5$). Their occurrence is found extremely sensitive to both Re and g with the existence of intermediate 'transition' regions of the parameter space where different solutions are obtained for the same values of g and Re. The same flow patterns have been described also by Liu *et al.* (2007) in addition to the steady symmetric flow at various gap sizes. Illustrative examples of these different flow regimes are given in figure 2 by means of computed DNS snapshots that represent (*a*) the single bluff-body, (*b*) the steady asymmetric, (*c*) the in-phase synchronized and (*d*) the antiphase synchronized patterns.

In order to understand the origin of these different flow patterns, theoretical and numerical stability analyses have been carried out at fairly low Reynolds numbers. As an example, Peschard & Le Gal (1996) proposed a simple model consisting of two coupled Landau equations while a global stability analysis has been performed by Akinaga & Mizushima (2005) and Mizushima & Ino (2008). These latter works, however, provide only a partial description of the stability properties of the flow. Moreover, most of the aforementioned numerical results were obtained on computational domains probably too small to accurately describe the stability diagram in the parameter space g–Re.

This fact motivated us to perform a new global stability analysis on the symmetric base flow in the parameter range of $0.1 \leqslant g \leqslant 3$ and $Re \leqslant 100$. The analysis is carried out in a two-dimensional framework consistently with previous numerical studies and experimental findings at low Reynolds numbers where three-dimensional effects have not been described (Williamson 1985; Peschard & Le Gal 1996; Xu, Zhou & So 2003). Notwithstanding, instability to three-dimensional perturbations can be expected for $g \leqslant 0.4$ and $Re > 100$ based on the secondary instability thresholds of the isolated cylinder wake (Barkley & Henderson 1996) and on the augmented characteristic

length scale of the single bluff-body flow. Note, however, that these values of Re fall outside of the assumed range of investigation and moreover a three-dimensional stability investigation is beyond the main concern of this study. Obtained results are compared with those of previous authors showing that significant changes in the stability diagram occurs. Then, our investigation is extended to consider the structural sensitivity of the unstable modes with respect to linearized perturbations and base-flow modifications. On the one hand, by resorting to the wavemaker analysis introduced by Giannetti & Luchini (2007), flow regions where the various instability mechanisms develop are identified. On the other hand, the structural sensitivity to base-flow variations is exploited to suppress simultaneously the two synchronized vortex shedding modes using two small cylinders as passive devices. For such a purpose, the same approach as employed by Pralits, Brandt & Giannetti (2010) is adopted and the effectiveness of the secondary cylinder placement is verified by means of DNS of the controlled flow.

2. Mathematical formulation

The two-dimensional flow of an incoming uniform stream past a pair of circular cylinders in side-by-side arrangement is investigated herein. The flow field is described using a Cartesian coordinate system in which the cylinder centres lie along the vertical y-axis and are symmetrically positioned with respect to the horizontal x-axis which is aligned with the flow direction (see figure 1). The fluid motion is governed by the unsteady incompressible Navier–Stokes equations

$$\begin{cases} \dfrac{\partial \boldsymbol{U}}{\partial t} + (\boldsymbol{U}\cdot\boldsymbol{\nabla})\boldsymbol{U} + \boldsymbol{\nabla} P - \dfrac{1}{Re}\nabla^2\boldsymbol{U} = \boldsymbol{0}, \\ \boldsymbol{\nabla}\cdot\boldsymbol{U} = 0, \end{cases} \tag{2.1}$$

which are made dimensionless using the cylinder diameter D^*, the velocity of the incoming stream U^*_∞ and the (constant) density ρ^*. The flow configuration is completely described by two non-dimensional parameters: the Reynolds number Re and the non-dimensional gap spacing between the cylinder surfaces g. In this context, the flow state is specified by the velocity vector field $\boldsymbol{U}(x, y, t)$, with components (U, V), and by the reduced pressure field $P(x, y, t)$. In order to study the onset of the various flow instabilities, we perform a global stability and sensitivity analysis on top of the two-dimensional steady, symmetric solution $\boldsymbol{Q}_b = \{\boldsymbol{U}_b, P_b\}$ of (2.1). In particular, the perturbation field $\boldsymbol{q} = \{\boldsymbol{u}, p\}$ is assumed to have a normal mode form $\boldsymbol{q}(x, y, t) = \hat{\boldsymbol{q}}(x, y)\exp(\sigma t)$, where $\sigma \in \mathbb{C}$ and $\hat{\boldsymbol{q}}(x, y)$ is the mode shape. The perturbation satisfies the linearized Navier–Stokes equations which, with appropriate homogeneous boundary conditions, define a generalized eigenvalue problem for σ. In the following, we briefly recall the main results of the stability and sensitivity analysis, since these concepts are well known among the scientific community and have been described in detail in many papers among which we specifically mention Giannetti & Luchini (2007), Sipp & Lebedev (2007), Giannetti, Camarri & Luchini (2010) and Lashgari *et al.* (2012).

When dealing with an hydrodynamic oscillator (Huerre & Rossi 1998), the structural sensitivity analysis of the underlying unstable global mode allows us to identify the so-called wavemaker region, where the instability mechanism acts and develops. This can be achieved by computing the sensitivity tensor

$$\boldsymbol{S}(x, y) = \frac{\hat{\boldsymbol{f}}^+(x, y)\hat{\boldsymbol{u}}(x, y)}{\displaystyle\int_\Omega \hat{\boldsymbol{f}}^+ \cdot \hat{\boldsymbol{u}}\,\mathrm{d}\Omega}, \tag{2.2}$$

and building a spatial map of its Frobenius norm at each point of the domain Ω (Giannetti & Luchini 2007). In the above expression, the notation $\hat{\boldsymbol{f}}^{+}\hat{\boldsymbol{u}}$ indicates the dyadic product between the direct mode $\hat{\boldsymbol{u}}$ and the adjoint mode $\hat{\boldsymbol{f}}^{+}$ which is solution of the adjoint linearized equations. More details on the derivation of the direct and adjoint equations and their boundary conditions are found in Giannetti & Luchini (2007). For a complete review on global mode analysis and computation see Theofilis (2011) and Luchini & Bottaro (2014).

The sensitivity analysis that leads to (2.2) is based on a structural perturbation that acts at the perturbation level only, providing the right tool to study and localize the instability mechanism. A similar analysis can be repeated by introducing the structural perturbation also at the base-flow level (see Marquet, Sipp & Jacquin 2008; Pralits *et al.* 2010, for details). Indeed such a perturbation produces a modification of the base flow which in turn affects the coefficients of the linearized Navier–Stokes operator and consequently leads to a drift of the eigenvalue in the stability problem. The study of the sensitivity to base-flow modifications is extremely useful for the design of effective passive control strategies apt to suppress or enhance the instability. As in the previous case the analysis leads to the definition of a sensitivity tensor which expresses the sensitivity with respect to base-flow modifications

$$\boldsymbol{S}_b(x,y)=\frac{\hat{\boldsymbol{f}}_b^{+}(x,y)\boldsymbol{U}_b(x,y)}{\displaystyle\int_{\Omega}\hat{\boldsymbol{f}}^{+}\cdot\hat{\boldsymbol{u}}\,\mathrm{d}\Omega}, \tag{2.3}$$

where $\boldsymbol{U}_b$ is the base flow velocity while the field $\hat{\boldsymbol{f}}_b^{+}$ denotes the solution of the forced adjoint base-flow equations (Pralits *et al.* 2010). As for the wavemaker, the sensitivity to structural base-flow variations can be investigated by evaluating at each point of the domain a suitable tensor norm of (2.3) to derive a sensitivity map.

3. Numerical method

The two-dimensional Navier–Stokes equations (2.1), their linearized version and the corresponding adjoint formulation are solved on the rectangular computational domain Γ_{out} which is illustrated in figure 1. The equations are discretized in conservative form on a Cartesian smoothly varying staggered grid using a standard second-order finite-difference scheme. An immersed boundary technique is employed to impose no-slip boundary conditions on the two cylinder surfaces while preserving the second-order accuracy of the discretization (see Giannetti & Luchini 2007, for further details). On Γ_{out} the fully nonlinear equations are supplemented by the same outlet conditions employed in Carini *et al.* (2014). At the inlet Γ_{in}, upper Γ_{top} and lower Γ_{bottom} boundaries the vorticity is set to zero while the component of the velocity normal to the boundary is required to approach the constant value at infinity as $1/r$. For the computation of the direct and adjoint perturbation fields, the same boundary conditions are applied in homogeneous form.

Given the spatial discretization of the governing equations with associated boundary conditions, three different problems are addressed from the numerical point of view. First, the steady version of (2.1) is solved by Newton iterations to compute the symmetric base flow for linear stability analyses. Second, the direct and adjoint global modes are calculated making use of the implicitly restarted Arnoldi method implemented in the ARPACK library (Lehoucq, Sorensen & Yang 1998) with a

	$\bar{C}_D$		C'_L		St	
Kang (2003)	1.434		0.271		0.164	
Present	1.409	(1.74 %)	0.262	(2.58 %)	0.163	(0.6 %)

TABLE 1. Comparison of DNS results for the in-phase synchronized vortex shedding regime at $g = 1.5$ and $Re = 100$ being $\bar{C}_D$ the mean drag coefficient, C'_L the maximum amplitude of the lift coefficient fluctuations and St the Strouhal number. Owing to vortex shedding synchronization, all of these quantities assume the same value for both cylinders. We give the difference in percentage terms in brackets.

shift-invert strategy. In addition, the LOCA library of continuation algorithms (Salinger *et al.* 2002) is used to track global mode neutral curves in the plane g–Re. Finally, for unsteady flow simulations, the semi-discretized nonlinear Navier–Stokes equations are advanced in time by the hybrid third-order Runge–Kutta/Crank–Nicolson scheme of Rai & Moin (1991). All of the required matrix inversions are performed by means of the sparse LU solver provided with the software package UMFPACK (Davis 2004).

The main results presented in this work are obtained on a domain Ω_c of length $L_x = 125$ in the streamwise direction and $L_y = 100$ in the cross-stream one. With reference to figure 1, the inlet, the outlet and the lateral boundaries are located at a distance from to origin $L_{in} = 50$, $L_{out} = 75$ and $L_s = 50$, respectively. The whole computational domain is discretized using 430×450 nodes with a grid clustering near the two cylinder surfaces. More precisely, a uniform mesh with the finest grid spacing of $\Delta x = \Delta y = 0.02$ is employed in the small rectangular subdomain $[-1, 1] \times [-2.5, 2.5]$ always enclosing the two cylinders for the considered range of gap sizes. Indeed the same Cartesian mesh is employed to perform all flow computations for $0.1 \leqslant g \leqslant 3$ by exploiting the geometrical flexibility of the immersed boundary technique. The results have been validated by varying both grid resolution and domain size: some of these tests are described in appendix A, confirming that good convergence is achieved.

For the unsteady flow simulations, a non-dimensional time step of $\Delta t = 0.03$ is used and the same validating test case employed by Kang (2003) is considered. Results in table 1 agree well with those of this author: small discrepancies can be ascribed to the different downstream extent of the computational domain in Kang's simulations ($L_{out} = 30$) and to different flow conditions imposed on the external boundary.

4. Linear stability analysis

4.1. *Base flow*

At very low Reynolds numbers, i.e. $Re < 20$, the flow past the two cylinders is steady and symmetric with respect to the x-axis (Kang 2003; Liu *et al.* 2007). As Re increases this flow becomes rapidly unstable with respect to two-dimensional perturbations (Akinaga & Mizushima 2005; Mizushima & Ino 2008). When the two cylinders are in close proximity, i.e. for $g < 0.2$, the steady flow is similar to that behind a single cylinder of approximately double size, showing the formation of a single large separated flow region just behind the two bodies; an example of this wake structure is illustrated in figure 3(*a*) for $g = 0.1$ and $Re = 30$ by means of base flow streamlines. As the gap size increases, the big recirculation bubble completely detaches from the cylinder surfaces and gradually moves downstream becoming thinner and weaker until it disappears. Meanwhile two tiny bubbles start

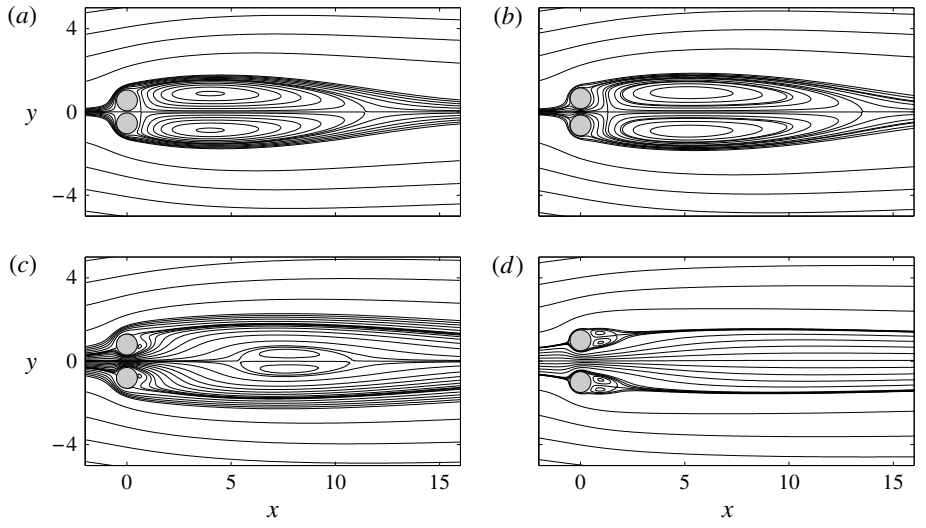

FIGURE 3. Symmetric base-flow patterns at $Re = 30$ for various gap sizes (streamlines). Single-body pattern at (*a*) $g = 0.1$ and (*b*) $g = 0.3$. (*c*) Intermediate 'transitional' pattern at $g = 0.6$. (*d*) Double-body pattern at $g = 1$.

to grow up on the rear–inner sides of the two cylinder surfaces, finally leading to the formation of two distinct wakes. The topological change from the single-body pattern, at small gap spacing, to the double-body pattern, at large gap spacing, is well described by the sequence of pictures in figure 3. It is worthwhile noting that the base flow transition occurs without any instability (Liu *et al.* 2007). In figure 3(*d*) the two wakes are shown to be weakly deflected on the external sides of the two cylinders due to the expansion of the internal flow passing through the gap. The deflection is expected to asymptotically reduce to zero in the limit of $g \to \infty$, for which wake interference is lost. Variations of the lift and drag coefficients C_L and C_D, respectively, as a function of the gap size ($Re = 30$) are illustrated in figure 4. Starting from $g = 0.1$ and increasing the separation of the two cylinders, both C_D and $|C_L|$ initially show a rapid variation that corresponds to an almost linear drag increment and a lift reduction. The trend occurs up to the approximate range of gap spacing where the base flow modifies from the single-body to the double-body pattern (grey shaded area). Further increasing the gap size, C_D gradually reaches a maximum value and afterwards starts to slowly decrease, while $|C_L|$ still continues to diminish but at a progressively smaller rate. The flow behaviour in these latter cases appears indeed consistent with an asymptotic trend to the single cylinder case ($C_D = 1.688$)

4.2. *Global modes*

Three harmonic modes and one steady antisymmetric mode are found to become unstable, each one being at the root of a distinct flow regime; for increasing gap size: single bluff-body vortex shedding (SB mode), asymmetric steady flow (AS mode) and in-phase/antiphase synchronized vortex shedding (IP/AP modes). The corresponding neutral curves are illustrated in the diagram of figure 5, thus circumscribing the domain of asymptotic stability of the symmetric base flow (dark grey shaded area). In particular, it can be noticed that for $g \sim 0.56$ the SB neutral curve shows a

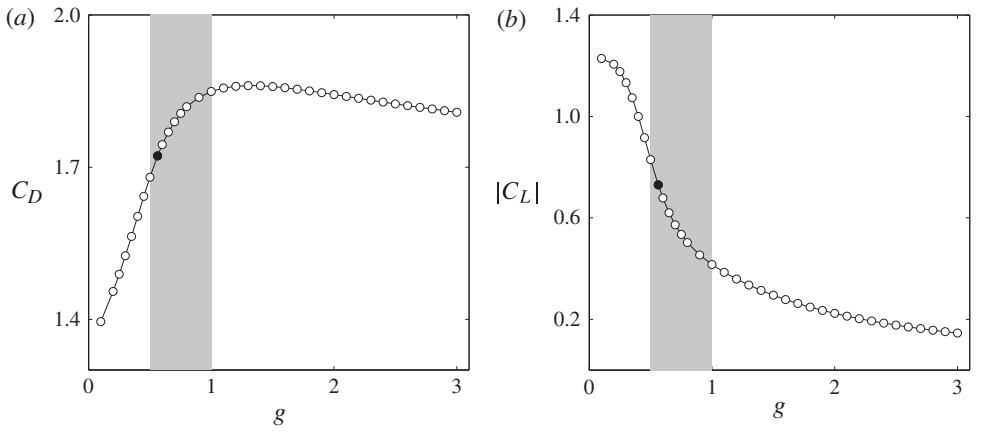

FIGURE 4. Base flow at $Re = 30$: aerodynamic coefficients as a function of g. (a) Drag coefficient C_D. (b) Lift coefficient C_L (absolute value). Both C_D and $|C_L|$ assume the same value for each cylinder since the base flow is symmetric. The grey shaded area denotes the approximate region of intermediate 'transitional' base-flow patterns (see also figure 3) while the black filled dot corresponds to the critical gap size of $g_c = 0.566$ associated with the instability threshold of the SB mode (see figure 5).

sudden upward bending reaching a nearly vertical slope: indeed as the base flow topology changes from the single-body to the double-body pattern, the SB mode must disappear, being related to the formation of a single wake structure. Three codimension-two bifurcation points are also located along the overall neutral curve (thick black line) at the intersections of neutral branches. These higher codimension bifurcations play a fundamental role in mode selection for intermediate values of the parameters between different flow regimes; however a nonlinear stability analysis is beyond the scope of the present investigation. An example of weakly-nonlinear analysis applied to the present configuration can be found in Carini *et al.* (2014) where a general technique based on centre-manifold reduction is explained and described in detail.

Results for the onset of the various flow instabilities are found consistent with previous studies by Akinaga & Mizushima (2005) and Mizushima & Ino (2008), although a detailed comparison indicates that non-negligible discrepancies affect the stability diagram. More precisely, the range of gap spacing associated with the occurrence of the pitchfork bifurcation driven by the AS mode instability is found markedly wider compared with that reported by Mizushima & Ino (2008) ($0.594 \leqslant g_c \leqslant 0.607$). In addition, the critical gap size of $g_c = 2.34$ for the IP–AP codimension-two bifurcation found by Akinaga & Mizushima (2005) is appreciably greater than the present value of $g_c = 1.875$. For these latter modes the stability analysis has been extended to large gap spacing and the computed critical values of Reynolds number and frequency are reported in table 2. The obtained results confirm the expected asymptotic trend: for $g \geqslant 10$ the two synchronized modes are characterized by almost coincident values of critical Re_c and frequency and for $g = 15$ IP and AP critical values are only slightly above those pertaining to the single cylinder wake (SC), i.e. $Re_c^{(SC)} \sim 46.5$ and $\mathrm{Im}(\sigma_c)^{(SC)} \sim 0.733$ (see also Giannetti & Luchini 2007; Marquet *et al.* 2008; Meliga & Chomaz 2011).

The described quantitative mismatch with the results of Akinaga & Mizushima (2005) and Mizushima & Ino (2008) has to be mainly ascribed to confinement effects

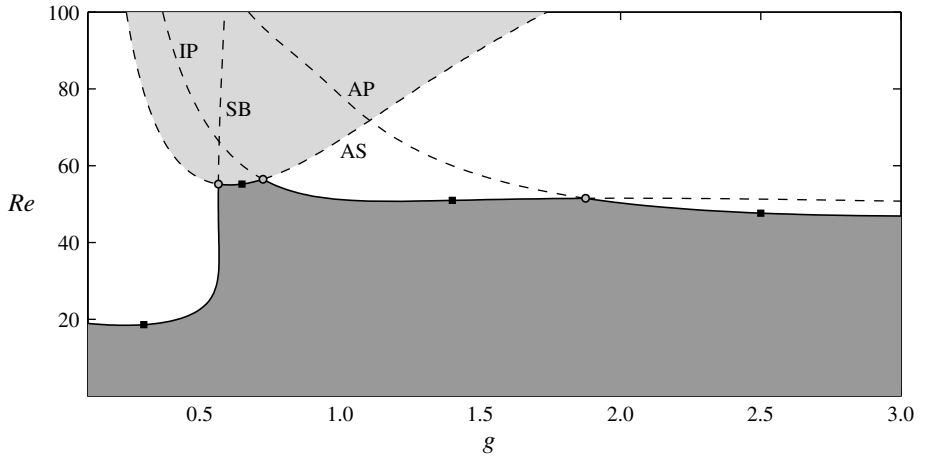

FIGURE 5. Linear stability diagram in the plane g–Re. The dark grey shaded area denotes the region of asymptotic stability of the symmetric base flow. The thick solid line represents the overall neutral curve along which the primary instability changes according to the neutral branches of the four global modes: SB ($g \leqslant 0.566$), AS ($0.566 \leqslant g \leqslant 0.725$), IP ($0.725 \leqslant g \leqslant 1.875$) and AP ($g \geqslant 1.875$). Thin dashed lines correspond to neutral branch continuation in the base flow unstable region. The domain of existence of the asymmetric steady solution is delimited by the AS mode neutral curve (light grey shaded area). Grey round dots are used to mark codimension-two bifurcations at the intersections of the neutral curves: SB–AS $(g_c, Re_c) = (0.566, 52.22)$, AS–IP $(g_c, Re_c) = (0.725, 56.46)$ and IP–AP $(g_c, Re_c) = (1.875, 51.52)$. Black square symbols denote marginally stable states assumed as reference solutions for global mode analysis: SB $(g_c, Re_c) = (0.3, 18.62)$, AS $(g_c, Re_c) = (0.65, 55.21)$, IP $(g_c, Re_c) = (1.4, 50.98)$ and AP $(g_c, Re_c) = (2.5, 47.65)$.

g	IP mode		AP mode	
	Re_c	$\mathrm{Im}(\sigma_c)$	Re_c	$\mathrm{Im}(\sigma_c)$
5	48.64	0.779	47.40	0.778
7	47.63	0.764	47.41	0.763
10	47.09	0.750	47.09	0.751
12	46.94	0.746	46.93	0.746
15	46.80	0.741	46.79	0.742

TABLE 2. Critical Reynolds number Re_c and mode frequency $\mathrm{Im}(\sigma_c)$ of IP and AP modes at large gap spacing. The computational grid has been adapted on purpose by enlarging the subdomain with uniform mesh size up to $[-1, 1] \times [-8.5, 8.5]$ with a maximum of $N_y = 1050$ grid points in the y direction.

induced by the small size of their employed computational domain. In order to assess the convergence of our stability results with respect to both the cross-stream extent of the domain and the grid resolution, stability computations have been repeated on different meshes confirming that adequate spatial convergence is achieved; see appendix A.

The computed global mode patterns at criticality (black square markers in figure 5) are illustrated in figure 6. In figure 6(*b*) the $\hat{u}$ component of the steady antisymmetric

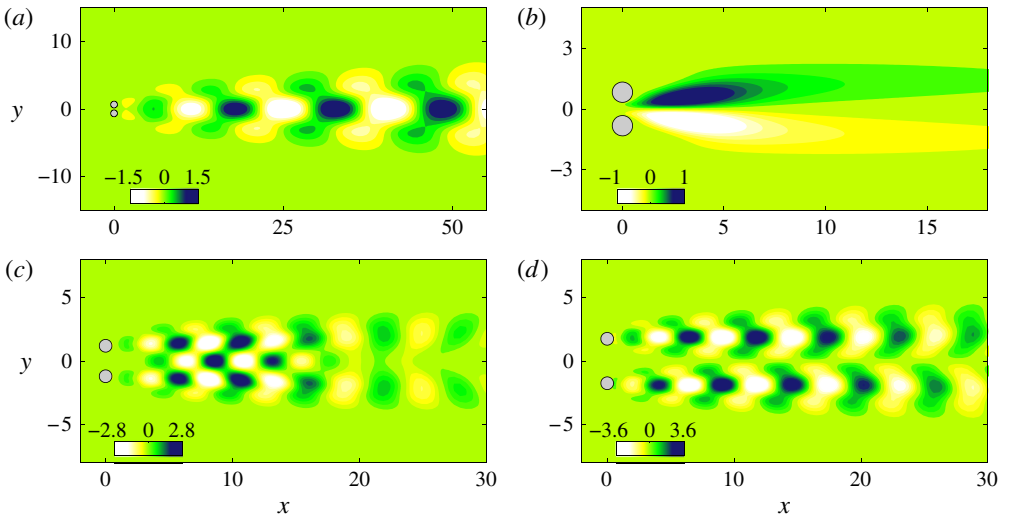

FIGURE 6. (Colour online) Marginally stable direct modes. (*a*) SB mode at $g_c = 0.3$ and $Re_c = 18.62$ (real part of the vorticity field). (*b*) AS mode at $g_c = 0.65$ and $Re_c = 55.21$ (real part of the $\hat{u}$ component). (*c*) IP mode at $g_c = 1.4$ and $Re_c = 50.98$ (real part of the vorticity field). (*d*) AP mode at $g_c = 2.5$ and $Re_c = 47.65$ (real part of the vorticity field).

(AS) mode is shown. As already mentioned, in this case the bifurcated flow state evolves towards an asymmetric steady solution of the governing equations (2.1) whose domain of existence is delimited by the AS neutral curve in figure 5 (light grey shaded area). An example of such asymmetric flow is depicted in figure 2(*b*) for $Re = 60$ and $g = 0.65$ (in this case the gap jet is deflected upward). For the SB mode, figure 6(*a*), the depicted vorticity field is clearly reminiscent of the single large-scale von Kármán vortex street developing above the critical SB threshold. Similarly, two parallel symmetric (antisymmetric) vortex rows characterize the IP (AP) mode pattern in figure 6(*c*,*d*). In particular, in the IP (symmetric) case a stronger interaction between the two wakes occurs. As is well known, during the in-phase synchronized vortex shedding the idealized symmetric double vortex street is progressively modified into a single large-scale street, the binary vortex street (Williamson 1985), owing to the pairing of vortices of the same sign. This process is illustrated in the DNS snapshot of figure 2(*c*). The same does not occur for the antiphase vortex shedding since vortices of the same sign do not pair-up.

For the oscillatory modes, variations of the mode frequency moving along the corresponding neutral curve are reported in figure 7. These frequency values are compared with those extracted from DNS. More precisely for $Re = 30$ and $g = 0.3$ the value of $St^{(SB)} = 0.0473$ pertaining to the unstable SB mode compares reasonably well with the shedding frequency $St = 0.0651$ computed from DNS. Similarly, for the in-phase synchronization of the two unsteady wakes at $g = 1.4$ and $Re = 60$, the IP mode frequency of $St^{(IP)} = 0.124$ provides a good estimate of the shedding frequency value of $St = 0.135$. On the other hand, during the antiphase regime at $g = 2.5$ and $Re = 80$ we found $St = 0.165$ while the value of $St^{(AP)} = 0.136$ is obtained from the stability analysis. The observed deviations of the shedding frequency from the corresponding linear stability predictions have to be ascribed to nonlinear effects which become more important as the Reynolds number is increased with respect to the critical one.

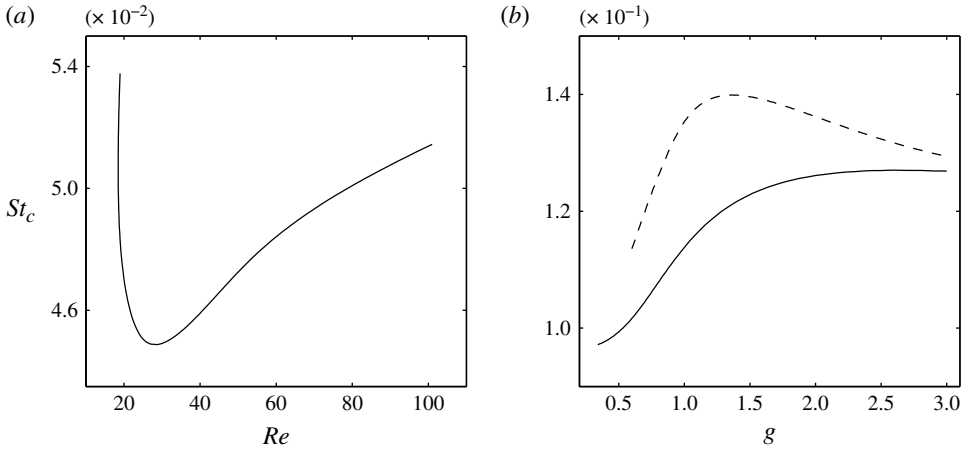

FIGURE 7. Variation of the critical frequency $St_c = \mathrm{Im}(\sigma_c)/2\pi$ associated with SB, IP and AP harmonic modes along the corresponding neutral curves of figure 5. (*a*) SB mode: St_c is plotted as a function of the critical Reynolds number Re_c. (*b*) IP (continuous line) and AP (dashed line) modes: St_c is plotted as a function of the critical gap size g_c.

5. Structural sensitivity

5.1. *Wavemaker investigation*

In this section the structural sensitivity of the critical modes (black square markers in figure 5) is analysed to locate the core region of the various instability mechanisms (Giannetti & Luchini 2007). The wavemaker structure associated with the SB mode is illustrated in figure 8(*a*). Similarly to the situation described by Giannetti & Luchini (2007), the norm of the sensitivity tensor is significantly different from zero only in the near-wake of the two cylinders and the core of the SB instability is located within two regions symmetrically placed at the rear–outer edges of the large separation bubble, where maximum values of sensitivity are observed. Structural sensitivity maps pertaining to the IP and AP modes are illustrated in figure 8(*c*,*d*), respectively. For these modes almost the same wavemaker structure of the SB mode and of the single cylinder wake can be recognized behind each cylinder. However, the sensitivity peaks behind each cylinder are not equal in magnitude: in the AP case stronger values are found on the gap sides, figure 8(*d*), while in the IP case they are located on the external sides, figure 8(*c*). We have checked that this property does not depend on g, thus suggesting that phase selection during vortex shedding synchronization is most influenced by different recirculating flow structures on the internal and external sides of the two steady wakes for the in-phase and antiphase synchronization, respectively.

Finally the sensitivity map associated with the AS mode is illustrated in figure 8(*b*): in this case the direct-adjoint product consists of two symmetric peaks located in the region between the two steady wakes. More precisely, the instability core is identified at the edges between the expanding gap flow and the rear–inner side of the two wake bubbles. Several analogies with the results of Fani, Camarri & Salvetti (2012) are observed. In this latter study the authors performed a stability and sensitivity analysis of the two-dimensional flow through a symmetric diffuser with an abrupt change of the channel cross-section. In analogy with the present case, the inherent symmetric base flow bifurcates to an asymmetric steady solution which is characterized by the

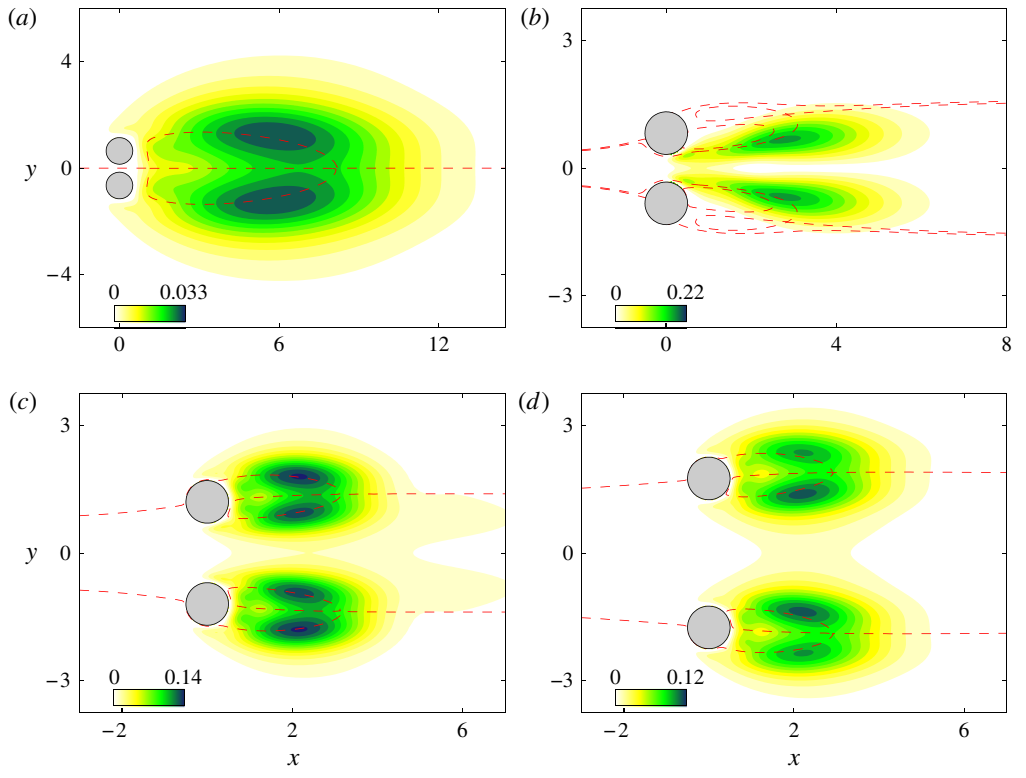

FIGURE 8. (Colour online) Structural sensitivity of the various marginally stable modes $\|\mathcal{S}\|_F$. Dashed lines are used to represents the limiting streamlines of the recirculating base-flow regions behind the two cylinders. (*a*) SB mode at $g_c = 0.3$ and $Re_c = 18.62$. (*b*) AS mode at $g_c = 0.65$ and $Re_c = 55.21$. (*c*) IP mode at $g_c = 1.4$ and $Re_c = 50.98$. (*d*) AP mode at $g_c = 2.5$ and $Re_c = 47.65$.

deflection of the expanding jet. This analogy may suggest that a similar physical mechanism of instability is involved in both cases.

5.2. *Passive control of synchronized shedding modes*

The simultaneous suppression of the IP and AP shedding modes is now investigated using two small control cylinders. Their effective placement is chosen according to the structural sensitivity of these modes with respect to unsteady perturbations and base-flow variations following the approach first introduced by Luchini, Pralits & Giannetti (2007) and Marquet *et al.* (2008) for the wake of a single cylinder and later employed by Pralits *et al.* (2010), Fani *et al.* (2012), Magri & Juniper (2013) and Pralits, Giannetti & Brandt (2013) for different flow configurations. Within such framework, the presence of an infinitely small control device is considered and modelled in terms of a localized feedback (drag) force

$$\delta \boldsymbol{F}(x, y) = -\delta F \delta(x - x_0, y - y_0) \boldsymbol{U}(x, y), \tag{5.1}$$

different formulae being available in the literature to estimate the coefficient δF; see for instance Pralits *et al.* (2010) and Fani *et al.* (2012). The introduced perturbation

results in an eigenvalue shift both directly at the linearized equations level by modifying the structure of the eigenvalue problem, and indirectly at the base flow level by modifying the steady solution from which the linearized Navier–Stokes operator depends. However, this latter effect is expected to be noticeably greater than the former (Luchini, Giannetti & Pralits 2008). The induced total eigenvalue drift $\delta\sigma_t$ can be written as

$$\delta\sigma_t = \delta\sigma + \delta\sigma_b = (\boldsymbol{S}_t : \boldsymbol{I})\delta F = \mathrm{Tr}(\boldsymbol{S}_t)\delta F \tag{5.2}$$

where $\delta\sigma_b$ is the eigenvalue drift due to a structural base-flow variation only and $\boldsymbol{S}_t = \boldsymbol{S} + \boldsymbol{S}_b$ is the total sensitivity tensor. The quantity $\mathrm{Tr}(\boldsymbol{S}_t)$ is a complex-valued function of the position (x_0, y_0) of the control device, which corresponds to the total eigenvalue drift for $\delta F = 1$. The real (imaginary) part of $\mathrm{Tr}(\boldsymbol{S}_t(x_0, y_0))$ can be used to build a spatial map of the mode growth-rate (frequency) sensitivity with respect to the position of the device, thus providing a useful guideline for the effective placement of small but finite control cylinders. Once the proper placement of the secondary cylinders has been chosen, its effectiveness can be checked by running a DNS of the controlled flow. In fact, by means of DNS we can also verify that no other modes are destabilized by the presence of the passive devices; at the same time we can account for nonlinear effects that have been neglected in the sensitivity framework.

Sensitivity maps pertaining to the IP and AP modes for $g = 2.5$ and $Re = 60$ are illustrated in figures 9 and 10, respectively. In order to describe the different contributions to the growth rate and the frequency variations, real and imaginary parts of $\mathrm{Tr}(\boldsymbol{S})$ and $\mathrm{Tr}(\boldsymbol{S}_b)$ have been illustrated separately. As expected, the sensitivity to base-flow modifications is found one order of magnitude greater than that to unsteady linear for both modes. The largest sensitivity to base-flow modifications is attained close to the cylinder surfaces on upper and lower sides. In particular, negative growth-rate variations are produced almost at the same spatial locations, thus providing a rationale for the simultaneous suppression of both modes. In order to achieve such result, two secondary control cylinders are employed with a symmetric placement with respect to the x-axis. In principle, it could be possible to use a single control device placed in the near-wake of one of the two main cylinders. However, preliminary tests have shown that when only one control cylinder is employed with such a positioning, vortex shedding is substantially reduced for the cylinder close to the control device but not for the other one, due to a destabilizing effect on other modes. At the same time, with reference to figures 9 and 10, the growth-rate sensitivity $\mathrm{Re}(\mathrm{Tr}(\mathcal{S}_b))$ reduces nearly to zero on the x-axis, thus preventing the symmetric placement of a single cylinder from being effective (at least for the considered value of g). Therefore, the choice of two identical control cylinders symmetrically placed with respect to the x-axis is adopted. In analogy to previous studies and based on computed values of global mode growth rates and on δF estimates, the secondary cylinder diameter is chosen equal to $d^* = 0.1D^*$. Two different stabilizing configurations are considered which are represented in figure 11 (black cylinders) superposed to IP and AP growth-rate sensitivity maps. In the first case, control cylinders are placed in the outer flow regions where a negative growth-rate variation is produced. In the second case, the control cylinders are placed in the analogous internal regions. Additional tests are performed by examining two configurations with control cylinders being placed on internal or external regions of positive growth-rate variations (small grey cylinders in figure 11). In all of these cases DNSs of the controlled flow are impulsively started from a uniform stream

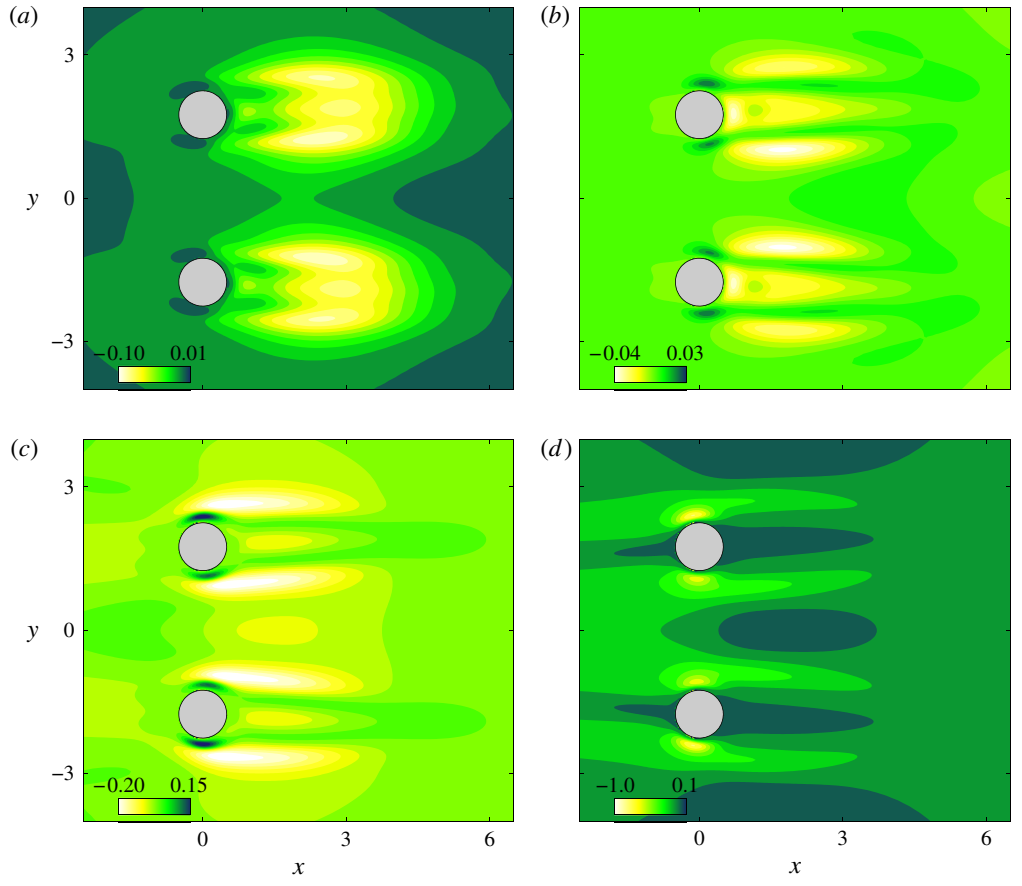

FIGURE 9. (Colour online) Structural sensitivity for the IP mode for $g = 2.5$ and $Re = 60$: (*a*,*c*) growth-rate and (*b*,*d*) frequency variation due to an infinitely small secondary cylinder with $\delta F = 1$. (*a*,*b*) Sensitivity to unsteady perturbations, $\mathrm{Tr}(\boldsymbol{S})$. (*c*,*d*) Sensitivity to base-flow modifications, $\mathrm{Tr}(\boldsymbol{S}_b)$.

while the two small control cylinders are treated using the same immersed boundary technique presented in § 3: a grid refinement has been introduced with the finest mesh size of $\Delta x = \Delta y = 0.01$ to properly resolve the flow details. In figure 12 time histories of the drag coefficients of the two main cylinders clearly indicate that for the stabilizing placement (black cylinders), synchronized vortex shedding is completely suppressed and a steady symmetric flow is realized. For the other two configurations (grey cylinders) obtained results are shown in figure 13. As expected, synchronized vortex shedding is not suppressed and an almost in-phase synchronization of the two wakes is found to occur in both cases.

6. Conclusions

The linear stability of the two-dimensional flow past two side-by-side circular cylinders is investigated within the parameter ranges of $0.1 \leqslant g \leqslant 3$ and $Re \leqslant 100$. Consistently with previous studies by Akinaga & Mizushima (2005) and Mizushima & Ino (2008), four distinct unstable modes are found and the related neutral curves are

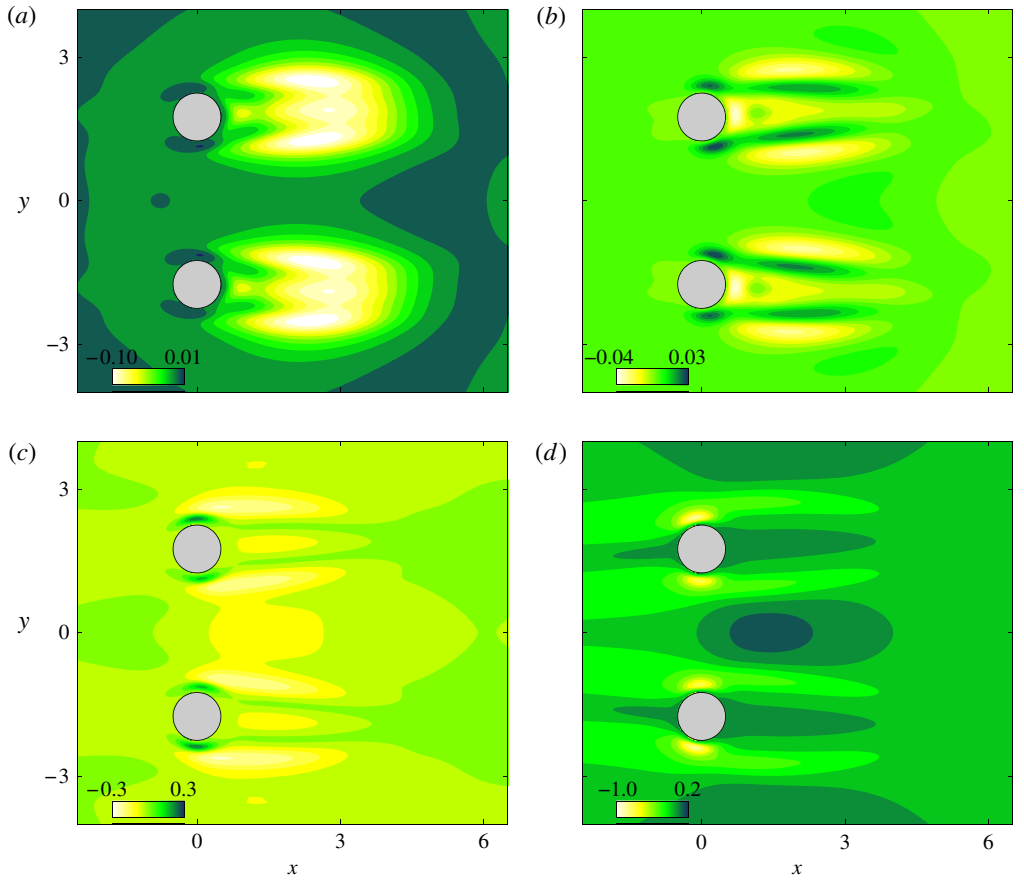

FIGURE 10. (Colour online) Structural sensitivity for the AP mode for $g = 2.5$ and $Re = 60$: (*a*,*c*) growth-rate and (*b*,*d*) frequency variation due to an infinitely small device with $\delta F = 1$. (*a*,*b*) Sensitivity to unsteady perturbations, $\mathrm{Tr}(\boldsymbol{S})$. (*c*,*d*) Sensitivity to base-flow modifications, $\mathrm{Tr}(\boldsymbol{S}_b)$.

described in the plane *g*–*Re*. Non-negligible quantitative discrepancies are noted by comparing the present stability diagram with those obtained by these authors which result in a different location of the neutral branches and of the codimension-two bifurcations points.

For leading global modes arising at different critical Reynolds numbers and gap sizes, both direct and adjoint eigenfunctions are computed to examine their sensitivity to structural modifications acting both at the perturbation level and at the base flow level. In particular, a wavemaker analysis is performed to identify the core region of the various instability mechanisms (Giannetti & Luchini 2007). Several analogies are observed with other globally unstable flows described in the literature. For the SB mode, the wavemaker structure corresponds to that of the isolated cylinder wake (Giannetti & Luchini 2007; Marquet *et al.* 2008). Similar features are found for the two synchronized shedding modes. In particular, maximum sensitivity is achieved at the external side of the recirculating base-flow regions for the IP mode and at the internal ones for the AP mode thus suggesting that these flow regions play a different role in the phase selection mechanism of the vortex shedding

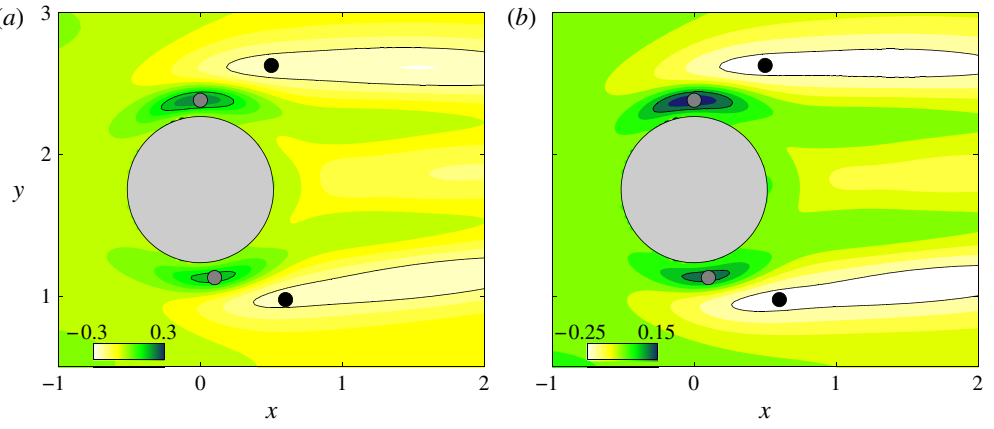

FIGURE 11. (Colour online) Control of synchronized vortex shedding at $Re = 60$ and $g = 2.5$: control cylinder placement superposed to total growth-rate sensitivity $\mathrm{Tr}(\boldsymbol{S}_t)$ of IP and AP modes. For each considered configuration only one control cylinder is shown, the control cylinder placement being symmetric with respect the x-axis. Black cylinders correspond to selected stabilizing inner and outer positions at $(x, y) = (0.6, 0.975)$ and $(x, y) = (0.5, 2.625)$, respectively. Grey cylinders correspond to selected inner and outer positions for which mode instability is enhanced with $(x, y) = (0, 2.38)$ and $(x, y) = (0.1, 1.13)$, respectively. (a) Total growth-rate sensitivity $\mathrm{Tr}(\boldsymbol{S}_t)$ for the IP mode: black contour lines correspond to $\mathrm{Tr}(\boldsymbol{S}_t) = -0.2$ and $\mathrm{Tr}(\boldsymbol{S}_t) = 0.15$. ($b$) Total growth-rate sensitivity $\mathrm{Tr}(\boldsymbol{S}_t)$ for the AP mode: black contour lines correspond to $\mathrm{Tr}(\boldsymbol{S}_t) = -0.2$ and $\mathrm{Tr}(\boldsymbol{S}_t) = 0.1$.

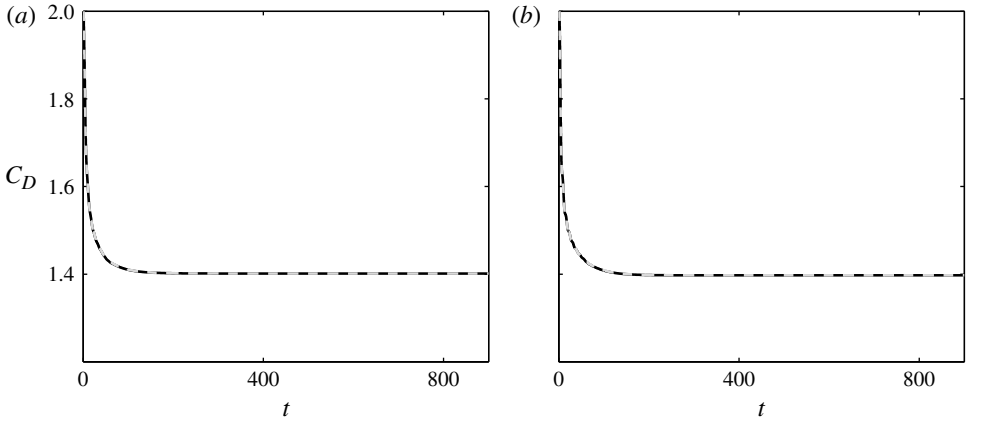

FIGURE 12. Passive control of synchronized shedding modes at $Re = 60$ and $g = 2.5$: stabilizing control cylinder placements. Drag coefficient histories of the two main cylinders are represented by black continuous and grey dashed lines. (a) Internal placement of the two control cylinders. (b) External placement of the two control cylinders; see also figure 11.

synchronization. For the AS mode the instability core is found approximately at the edges between the expanding gap flow and the two steady wakes, showing a strong analogy with the results described by Fani *et al.* (2012) for the asymmetric instability of a two-dimensional channel flow with a sudden expansion.

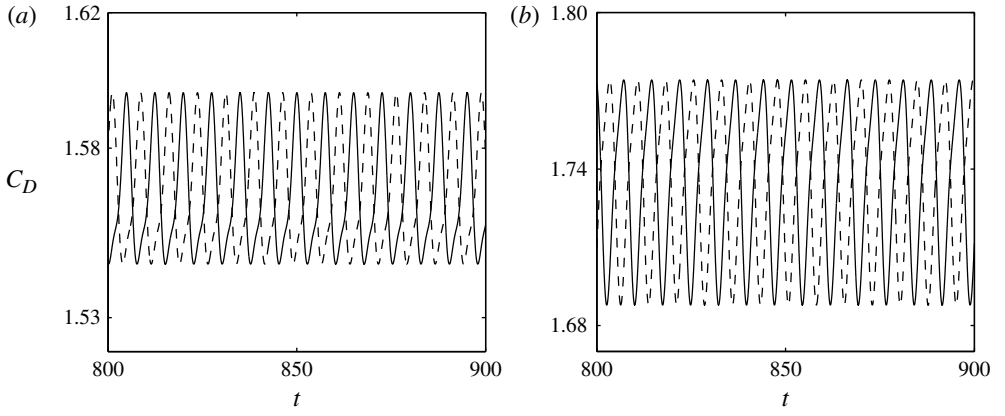

FIGURE 13. Passive control of synchronized shedding modes at $Re = 60$ and $g = 2.5$: inner placement of the two control cylinders enhancing the two unstable modes IP and AP, see also figure 11. Drag coefficient histories for the two main cylinders are represented by black continuous and dashed lines. (*a*) Internal placement of the two control cylinders. (*b*) External placement of the two secondary cylinders. See also figure 11.

The structural sensitivity analysis of the IP and AP modes with respect to base-flow modifications has been employed to design a passive control of these unstable modes for $g = 2.5$ and $Re = 60$. Following the approach of Pralits *et al.* (2010), two small secondary cylinders are symmetrically positioned with respect to the x-axis on the inner or on the outer cylinder sides, where mode quenching is induced and thus effective passive control can be achieved. This is confirmed *a posteriori* by means of DNS, showing that a steady symmetric flow is obtained in the controlled case and no other modes are destabilized.

It is worthwhile to notice that the unsteady asymmetric patterns described by Kang (2003) such as the deflected oscillatory pattern can find only a partial interpretation based on the present stability analysis. These patterns are indeed supposed to develop as secondary instabilities on the steady asymmetric base flow: preliminary results concerning the global stability analysis of this base flow are briefly presented in the appendix B. In addition, mode selection that occurs at intermediate values of g between regions associated with different flow regimes (Kang 2003) cannot be completely explained in terms of the linear picture alone. For these regions where multiple modes show nearly the same critical threshold and become unstable, a nonlinear analysis is needed to tackle the problem of competing instabilities (Meliga, Gallaire & Chomaz 2012). Within such a framework codimension-two bifurcations points reported in figure 5 play a central role and a weakly nonlinear analysis can be performed in the neighbourhood of these points to shed light on the underlying nonlinear mechanisms of mode selection. Both the above subjects will be considered in future studies of this flow.

Appendix A. Sensitivity of the results to domain size and grid resolution

The described quantitative mismatch with the results of Akinaga & Mizushima (2005) and Mizushima & Ino (2008) has to be mainly ascribed to confinement effects induced by the small size of their employed computational domain. More precisely, in both cases the box size in the direction normal to the main stream appears too small

	M_0	M_1	M_2	M_3	M_4
L_s	50	40	30	20	10
N_y	450	430	410	390	370

TABLE 3. Different meshes employed to investigate cross-wise flow confinement effects on stability results. Only L_s and the number of grid points in the y direction N_y are varied while L_{in}, L_{out} and the number of grid points in the x direction N_x are kept fixed to the values indicated in § 3, i.e. $L_{in} = 50$, $L_{out} = 75$ and $N_x = 430$. Here M_0 denotes the mesh used to produce the main stability results presented in this work.

	SB mode		AS mode	IP mode		AP mode	
	Re_c	$\mathrm{Im}(\sigma_c)$	Re_c	Re_c	$\mathrm{Im}(\sigma_c)$	Re_c	$\mathrm{Im}(\sigma_c)$
M_0	18.62	0.3100	55.20	50.98	0.764	47.64	0.832
M_1	18.59	0.3102	55.12	50.90	0.766	47.59	0.833
M_2	18.54	0.3109	54.95	50.80	0.767	47.49	0.834
M_3	18.48	0.3089	54.58	50.67	0.766	47.41	0.833
M_4	18.49	**0.287**	**52.66**	50.50	**0.742**	47.43	**0.81**

TABLE 4. Variations of the critical Reynolds number Re_c and frequency $\mathrm{Im}(\sigma_c)$ on meshes M_0–M_4 for the different unstable global modes. For each mode, the gap size is kept fixed to the value associated with the black square symbol on the corresponding neutral curve of figure 5.

to get a converged approximation of the stability properties of the unconfined flow field with $L_s \sim 10$. In order to support this interpretation, the eigenvalue sensitivity to the cross-stream extent of Ω_c has been briefly investigated herein. This has been done by performing stability computations on four additional meshes (M_1–M_4) with reduced L_s size; related properties are summarized in table 3. For each mode, g is kept fixed to the value associated with the corresponding black square symbol in figure 5. Then the critical Reynolds number and frequency are computed on domains M_1–M_4, thus providing a measure of the sensitivity of the stability results with respect to L_s. With reference to table 4, computed values of Re_c and $\mathrm{Im}(\sigma_c)$ are almost insensitive to the cross-wise extent of the domain down to a minimum size of $L_s = 10$ for which small but non-negligible deviations are shown to affect either the critical frequency for the SB, IP and AP modes and the critical Reynolds number for the AS mode. Finally, to assess the convergence of our stability results with respect to grid resolution, eigenvalue computations have been repeated on a refined mesh M_R with a minimum grid spacing of $\Delta x = \Delta y = 0.01$ and a total of 650×800 grid points. Obtained results on meshes M_0 and M_F are compared in table 5. Roughly speaking, this test shows that eigenvalue convergence to at least three significant digits is achieved.

Appendix B. Secondary instabilities on the asymmetric steady flow

As mentioned in the introduction, the steady asymmetric flow defines a steady solution of (2.1) for values of Re and g above the AS mode critical threshold (light grey area in figure 5). A preliminary stability analysis of this base flow indicates that at least two unstable vortex shedding modes exist which are referred to as the asymmetric in-phase (AIP) shedding mode and the far-wake single (FWS) shedding

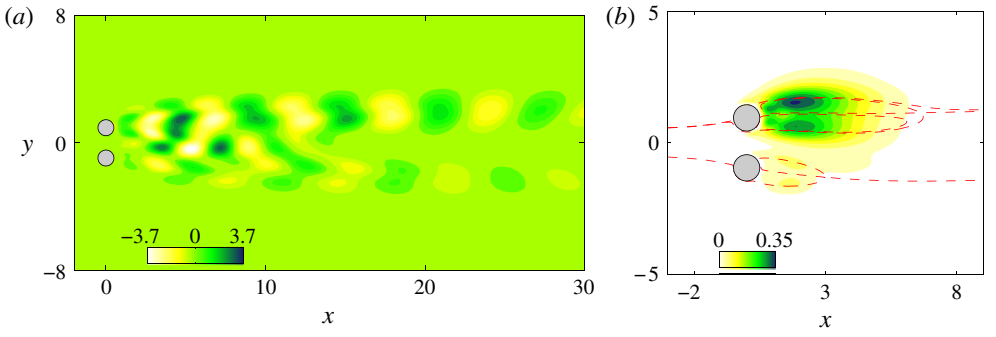

FIGURE 14. (Colour online) Marginally stable AIP mode at $(g_c, Re_c) = (0.9, 66.12)$ (asymmetric base flow). (*a*) Direct mode (real part of the vorticity field). (*b*) Structural sensitivity $\|\mathcal{S}\|_F$.

	M_0	M_R
SB mode	$3.2 \times 10^{-12} + 0.3097\mathrm{i}$	$-1.1 \times 10^{-4} + 0.3098\mathrm{i}$
AS mode	-2.8×10^{-7}	4.7×10^{-5}
IP mode	$7.7 \times 10^{-13} + 0.7646\mathrm{i}$	$-5.1 \times 10^{-4} + 0.7649\mathrm{i}$
AP mode	$6.3 \times 10^{-12} + 0.8316\mathrm{i}$	$-5.4 \times 10^{-4} + 0.8322\mathrm{i}$

TABLE 5. Values of σ computed using the standard mesh M_0 and the refined mesh M_R having a minimum grid size of $\Delta x = \Delta y = 0.01$ and a total of 650×800 grid points. In both cases the spatial extent of the computational domain Ω_c is the same. For each mode, the computations are performed at critical values of Re and g associated with the black square marker on the neutral curve of figure 5.

mode. The vorticity pattern of the marginally stable AIP mode is shown in figure 14(*a*) for $g_c = 0.9$ and $Re_c = 66.12$. In the present computations, the base flow is given with a downward gap flow deflection that is opposite to what illustrated in figure 2(*b*). For the considered mode an approximate in-phase vortex shedding takes place behind the two cylinders with a critical frequency of $St_c^{(AIP)} = 0.1032$ which is close to that of the IP mode for the same gap size ($St_c^{(IP)} = 0.111$). However, due to the inherent asymmetry of the basic state, a stronger vortex street is formed behind the upper cylinder and moving downstream the mode pattern is rapidly modified resulting into two asymmetric, out-of-phase vortex rows. The associated sensitivity map $\|\mathcal{S}\|_F$ is illustrated in figure 14(*b*). The wavemaker structure is markedly asymmetric compared with those of the IP and AP modes (see figure 8) and the location of the sensitivity maxima suggests the dominant role of the upper cylinder wake for the onset of the instability.

The critical FWS mode is illustrated in figure 15(*a*) for $g_c = 0.7$ and $Re_c = 67.98$. The depicted vorticity field (real part) corresponds to a single von Kármán street developing from the upper cylinder and reaching the far-wake region close to the outflow boundary where a large-scale vortex row is formed and mode maxima are located. The development of a single vortex street from the upper cylinder is confirmed by the unsteady flow simulations: in the DNS snapshot of figure 15(*b*) ($g = 0.7$ and $Re = 75$) the small wake bubble behind the lower cylinder simply

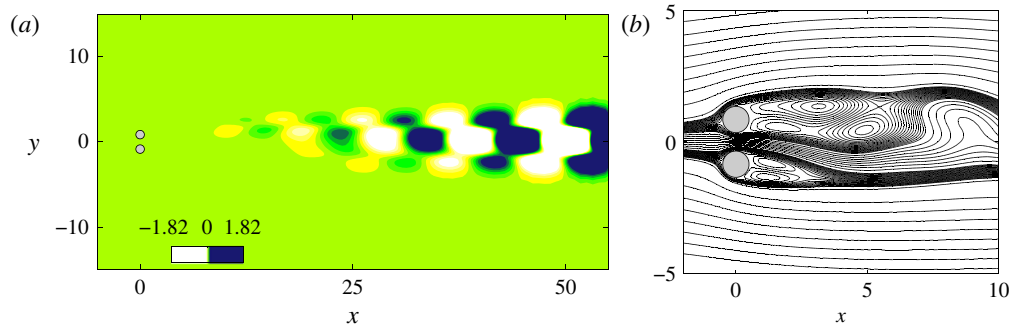

FIGURE 15. (Colour online) FWS mode (asymmetric base flow). (*a*) Direct mode at criticality, $(g_c, Re_c) = (0.7, 67.98)$ (real part of the vorticity field). (*b*) DNS snapshot at $g = 0.7$ and $Re = 75$ (streamlines).

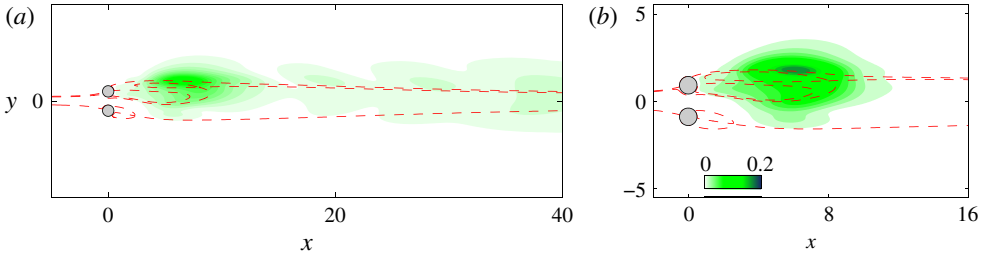

FIGURE 16. (Colour online) Structural sensitivity of the marginally stable FWS mode $\|\mathcal{S}\|_F$: (*a*) $(g_c, Re_c) = (0.7, 67.98)$; (*b*) $(g_c, Re_c) = (0.8, 67.93)$.

oscillates without breaking; the same behaviour has been experimentally observed by Xu *et al.* (2003) for $g = 0.4$ and $Re = 150$. The corresponding sensitivity map is depicted in figure 16 for two different values of the gap spacing. It is worthwhile to notice that differently from the AIP mode and from the reference results for the single cylinder wake (Giannetti & Luchini 2007), the wavemaker structure of the FWS mode is characterized by a single sensitivity peak which is located across the rear upper part of the long recirculating wake bubble. For $g_c = 0.8$ and $Re_c = 67.93$, figure 16(*b*), the wavemaker structure is highly localized in space thus allowing the correct identification of the 'instability core' associated with the FWS mode. However, for $g_c = 0.7$ and $Re_c = 67.98$, figure 16(*a*), small but non-negligible values of $\|\mathcal{S}\|_F$ are still found moving downstream to the outflow boundary, thus producing a lack of convergence of the considered mode with respect to the downstream extent of the computational domain, even for the longest domain employed here. Even if the physical relevance of the FWS mode is confirmed by the experimental results of Xu *et al.* (2003), more efforts are required to clarify the nature of the obtained sensitivity results, to understand whether they are a pure numeric artifact related to the downstream location of the outflow boundary or whether they are related to a possible coupling mechanism between the near-wake and the far-wake. In addition, other global modes are expected to become unstable within the domain of existence of the asymmetric base flow. All of these issues will be considered in a future study focused on these secondary instabilities.

REFERENCES

AFGAN, I., KAHIL, Y., BENHAMADOUCHE, S. & SAGAUT, P. 2011 Large eddy simulation of the flow around single and two side-by-side cylinders at subcritical Reynolds numbers. *Phys. Fluids* **23**, 075101.

AKINAGA, T. & MIZUSHIMA, J. 2005 Linear stability of flows past two circular cylinders in a side-by-side arrangement. *J. Phys. Soc. Japan* **74** (5), 1366–1369.

ALAM, M. M., MORIYA, M. & SAKAMOTO, H. 2003 Aerodynamic characteristics of two side-by-side circular cylinders and application of wavelet analysis on the switching phenomenon. *J. Fluids Struct.* **23**, 325–346.

ALAM, M. M. & ZHOU, Y. 2007 Flow around two side-by-side closely spaced circular cylinders. *J. Fluids Struct.* **18**, 799–805.

BARKLEY, D. & HENDERSON, R. D. 1996 Three-dimensional floquet stability analysis of the wake of a circular cylinder. *J. Fluid Mech.* **322**, 215–241.

BEARMAN, P. W. & WADCOCK, A. J. 1973 The interaction between a pair of circular cylinders normal to a stream. *J. Fluid Mech.* **61**, 499–511.

CARINI, M., GIANNETTI, F. & AUTERI, F. 2014 On the origin of the flip-flop instability of two side-by-side cylinder wakes. *J. Fluid Mech.* **742**, 552–576.

CARINI, M., AUTERI, F. & GIANNETTI, F. 2014 Centre-manifold reduction of bifurcating flows. *J. Fluid Mech.* (submitted).

CHEN, L., TU, J. Y. & YEOH, G. H. 2003 Numerical simulation of turbulent wake flows behind two side-by-side cylinders. *J. Fluids Struct.* **18**, 387–403.

DAVIS, T. A. 2004 Algorithm 832: UMFPACK, an unsymmetric-pattern multifrontal method. *ACM Trans. Math. Softw.* **30** (2), 196–199.

FANI, A., CAMARRI, S. & SALVETTI, M. V. 2012 Stability analysis and control of the flow in a symmetric channel with a sudden expansion. *Phys. Fluids* **24**, 084102.

GIANNETTI, F., CAMARRI, S. & LUCHINI, P. 2010 Structural sensitivity of the secondary instability in the wake of a circular cylinder. *J. Fluid Mech.* **651**, 319–337.

GIANNETTI, F. & LUCHINI, P. 2007 Structural sensitivity of the first instability of the cylinder wake. *J. Fluid Mech.* **581**, 167–197.

HUERRE, P. & ROSSI, M. 1998 Hydrodynamic instabilities in open flows. In *Hydrodynamics and Nonlinear Instabilities* (ed. C. Godrèche & P. Manneville), pp. 81–294. Cambridge University Press.

ISHIGAI, S., NISHIKAWA, E., NISHMURA, K. & CHO, K. 1972 Experimental study on structure of gas flow in tube banks with tube axes normal to flow: Part 1, Kármán vortex flow around two tubes at various spacings. *Bull. JSME* **15**, 949–956.

JESTER, W. & KALLINDERIS, Y. 2003 Numerical study of the incompressible flow about a fixed cylinder pairs. *J. Fluids Struct.* **17**, 561–577.

KANG, S. 2003 Characteristics of flow over two circular cylinders in a side-by-side arrangement at low Reynolds numbers. *Phys. Fluids* **15**, 2486–2498.

LASHGARI, I., PRALITS, J. O., GIANNETTI, F. & BRANDT, L. 2012 First instability of the flow of shear-thinning and shear-thickening fluids past a circular cylinder. *J. Fluid Mech.* **701**, 201–227.

LEHOUCQ, R. B., SORENSEN, D. C. & YANG, C. 1998 *ARPACK Users Guide*. SIAM.

LIU, K., MA, D. -J., SUN, D. -J. & YIN, X. -J. 2007 Wake patterns of flow past a pair of circular cylinders in side-by-side arrangements at low Reynolds numbers. *J. Hydrodyn.* B **19** (6), 690–697.

LUCHINI, P. & BOTTARO, A. 2014 Adjoint equations in stability analysis. *Annu. Rev. Fluid Mech.* **46**, 493–517.

LUCHINI, P., GIANNETTI, F. & PRALITS, J. O. 2008 Structural sensitivity of linear and nonlinear global modes. In *Proceedings of the 5th AIAA Theoretical Fluid Mechanics Conference, 23–26 June, Seattle, WA*, pp. 1–19. Curran Associates Inc.

LUCHINI, P., PRALITS, J. O. & GIANNETTI, F. 2007 Structural sensitivity of the finite-amplitude vortex shedding behind a circular cylinder. In *Proceedings of the 2nd IUTAM Symposium on*

Unsteady Separated Flows and Their Control, 18–22 June 2007, Corfu, Greece (ed. M. Braza & K. Houringan), pp. 151–160. Springer.

MAGRI, L. & JUNIPER, M. P. 2013 Sensitivity analysis of a time-delayed thermo-acoustic system via an adjoint-based approach. *J. Fluid Mech.* **719**, 183–202.

MARQUET, O., SIPP, D. & JACQUIN, L. 2008 Sensitivity analysis and passive control of cylinder flow. *J. Fluid Mech.* **615**, 221–252.

MELIGA, P. & CHOMAZ, J. -M. 2011 An asymptotic expansion for the vortex-induced vibrations of a circular cylinder. *J. Fluid Mech.* **671**, 137–167.

MELIGA, P., GALLAIRE, F. & CHOMAZ, J. -M. 2012 A weakly nonlinear mechanism for mode selection in swirling jets. *J. Fluid Mech.* **699**, 216–262.

MENEGHINI, J. R., SALTARA, F., SIQUEIRA, C. L. R. & FERRARI, J. A. 2001 Numerical simulation of flow interference between two circular cylinders in tandem and side-by-side arrangements. *J. Fluids Struct.* **15**, 327–350.

MIZUSHIMA, J. & INO, Y. 2008 Stability of flows past a pair of circular cylinders in a side-by-side arrangement. *J. Fluid Mech.* **595**, 491–507.

PESCHARD, I. & LE GAL, P. 1996 Coupled wakes of cylinders. *Phys. Rev. Lett.* **77**, 3122–3125.

PRALITS, J. O., BRANDT, L. & GIANNETTI, F. 2010 Instability and sensitivity of the flow around a rotating circular cylinder. *J. Fluid Mech.* **650**, 1–24.

PRALITS, J. O., GIANNETTI, F. & BRANDT, L. 2013 Three-dimensional instability of the flow around a rotating circular cylinder. *J. Fluid Mech.* **730**, 5–18.

RAI, M. M. & MOIN, P. 1991 Direct simulations of turbulent flow using finite-difference schemes. *J. Comput. Phys.* **96**, 15–53.

SALINGER, A. G., BOU-RABEE, N. M., PAWLOWSKI, R. P., WILKES, E. D., BURROUGHS, E. A., LEHOUCQ, E. A. & ROMERO, L. A. 2002 LOCA 1.1 – library of continuation algorithms: theory and implementation manual *Tech. Rep.* SAND2002-0396. Sandia National Laboratories.

SHAO, J. & ZHANG, C. 2008 Large eddy simulation of the flow past two side-by-side circular cylinders. *Intl J. Comput. Fluid Dyn.* **22** (6), 393–404.

SIPP, D. & LEBEDEV, A. 2007 Global stability of base and mean flows: a general approach and its applications to cylinder and open cavity flows. *J. Fluid Mech.* **593**, 333–358.

SPIVACK, H. M. 1946 Vortex frequency and flow pattern in the wake of two parallel cylinders at varied spacings normal to an airstream. *J. Aero. Sci.* **13**, 289–297.

SUMNER, D. 2010 Two circular cylinders in cross-flows: a review. *J. Fluids Struct.* **26**, 849–899.

SUMNER, D., WONG, S. S. T., PRICE, S. J. & PAÏDOUSSIS, M. P. 1999 Fluid behavior of side-by-side circular cylinders in steady cross-flow. *J. Fluids Struct.* **13**, 309–338.

THEOFILIS, V. 2011 Global linear instability. *Annu. Rev. Fluid Mech.* **43**, 319–352.

WILLIAMSON, C. H. K. 1985 Evolution of a single wake behind a pair of bluff bodies. *J. Fluid Mech.* **159**, 1–18.

XU, S. J., ZHOU, Y. & SO, R. M. C. 2003 Reynolds number effects on the flow structure behind two side-by-side cylinders. *Phys. Fluids* **15**, 1214–1219.

ZDRAVKOVICH, M. M. & PRIDDEN, D. L. 1977 Interference between two circular cylinders; series of unexpected discontinuities. *J. Wind Engng Ind. Aerodyn.* **2**, 255–270.

ZHOU, Y., ZHANG, H. J. & YIU, M. W. 2002 The turbulent wake of two side-by-side circular cylinders. *J. Fluid Mech.* **458**, 303–332.